Progress In Electromagnetics Research C, Vol. 172, 195–205, 2026 PIER C

(Received 20 April 2026, Accepted 25 May 2026, Scheduled 5 August 2026)

Compact Dual-Port MIMO Microstrip Patch Antenna with SRR Superstrate and Hybrid Defected Ground Structure for Multiband C/X-Band Applications

Arun R. Velraj*, Benny H. M. Johnson, and Merlise Rajan

Department of Electronics and Communication Engineering
Mepco Schlenk Engineering College, Sivakasi 626005, Tamil Nadu, India

ABSTRACT: This paper presents the design, simulation, fabrication, and experimental S-parameter validation of a compact dual-port multiple-input multiple-output (MIMO) microstrip patch antenna integrating a split-ring resonator (SRR) superstrate with a hybrid defected ground structure (DGS) for multiband C/X-band satellite uplink and radar applications. The antenna is implemented on an FR-4 substrate ($\varepsilon_r = 4.4$, $\tan\delta = 0.02$, $h = 1.6$ mm) with a compact footprint of $40 \times 40\,\text{mm}^2$. A 10×8 array of SRR unit cells positioned at 7 mm air gap above the radiating patches serves as a periodic frequency-selective superstrate to enhance gain via Fabry-Perot cavity resonance and suppress surface waves. Hybrid H-shaped and dumbbell-shaped DGS slots etched on the ground plane provide high isolation between ports by disrupting ground current paths and introducing bandstop characteristics. The simulated antenna resonates at 7.20, 8.62, and 10.66 GHz with return loss below -10 dB and isolation better than -20 dB in the operating bands. The fabricated prototype was tested using a vector network analyzer, and the measured S-parameters show good agreement with the simulations, with small shifts due to fabrication tolerances, SMA soldering, FR-4 dielectric variation, and air-gap alignment. Radiation patterns and gain are reported from HFSS simulation, whereas S-parameters are experimentally validated.

1. INTRODUCTION

1.1. Background and Motivation

The exponential growth of wireless communication systems, satellite networks, and radar applications has created an urgent demand for compact, high-performance antennas capable of operating across multiple frequency bands with enhanced data throughput and reliability [1, 2]. Multiple-input multiple-output (MIMO) technology has emerged as a cornerstone solution for next-generation wireless systems, offering significant improvements in channel capacity, spectral efficiency, and link reliability without requiring additional bandwidth or transmit power [3, 4]. According to Shannon's capacity theorem, MIMO systems can theoretically achieve an N-fold capacity increase for N uncorrelated antenna elements, making them essential for 5G/6G communications, satellite terminals, and phased-array radar systems.

However, the practical implementation of MIMO antennas faces critical challenges in compact form factors where mutual coupling between closely spaced radiating elements severely degrades diversity performance. Mutual coupling arises primarily from two mechanisms: (1) surface wave propagation along the substrate, dominant at higher frequencies (C-band and X-band), and (2) direct electromagnetic coupling through near-field interactions. This leads to degraded ECC, reduced diversity gain, and compromised channel capacity [5, 6].

* Corresponding author: Arun Raj Velraj (arunraj@mepcoeng.ac.in).

1.2. Prior Art and Limitations

Various techniques have been proposed to reduce mutual coupling in compact MIMO antennas, including defected ground structures, electromagnetic band-gap structures, parasitic elements, neutralization structures, metamaterial resonators, and superstrate-based decoupling methods [7–16]. Pouyanfar et al. [14] proposed a compact C/X-band MIMO antenna using DGS and reported improved isolation in both C- and X-band operating regions. Khan et al. [15] used a ground stub and an EBG structure to improve isolation in a compact wideband MIMO antenna. Karthigaiveni et al. [16] demonstrated an X-band MIMO antenna using a complementary split-ring resonator (CSRR)-loaded superstrate with high isolation and low envelope correlation coefficient (ECC). Tighilt et al. [17] reported a compact UWB-MIMO antenna using parasitic elements and CSRR-based ground modification to improve bandwidth and mutual coupling performance.

Recent metamaterial [28, 30, 31] and SRR-based MIMO antennas [26, 27] have also shown promising isolation and diversity characteristics. Undrakonda et al. [4] reported a compact C/X-band MIMO antenna with metamaterial-based decoupling, isolation greater than 20 dB, ECC below 0.1, and diversity gain of 9.98 dB. However, most existing works focus either on isolation enhancement or bandwidth improvement, and fewer works integrate SRR superstrate and hybrid DGS in a compact dual-port structure for simultaneous multiband operation, isolation improvement, and gain enhancement.

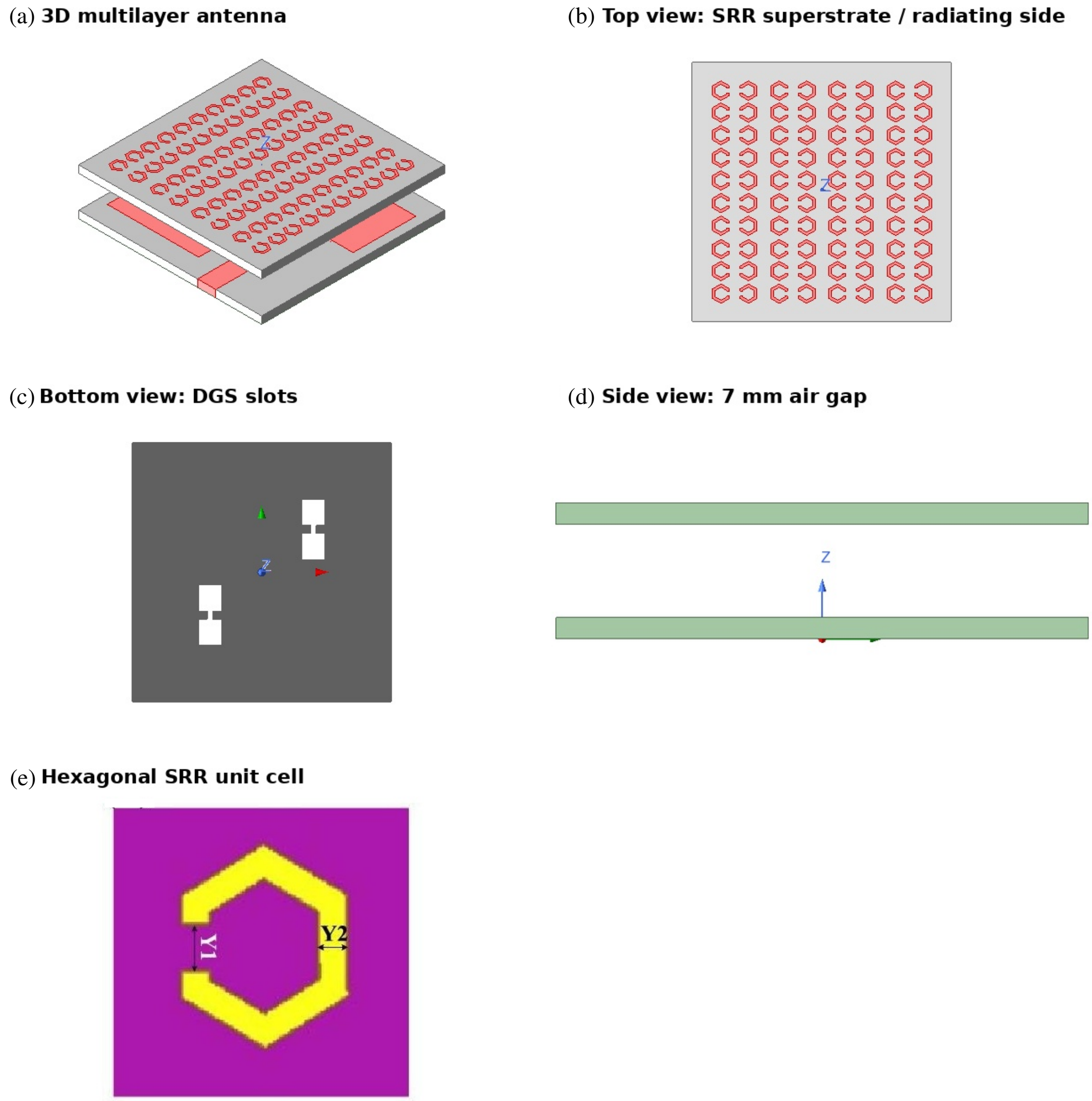

FIGURE 1. Proposed MIMO antenna geometry: (a) 3D multilayer view, (b) top view showing hexagonal SRR array/radiating side, (c) bottom view showing DGS slots, (d) side view showing 7 mm air gap, and (e) hexagonal SRR unit cell.

1.3. Research Gap and Motivation

Despite significant progress, existing C/X-band MIMO antennas face several critical limitations: (1) Trade-off between isolation and gain — DGS-based designs achieve high isolation but moderate gain (3–5 dBi), while superstrate-based designs achieve high gain but do not address MIMO isolation. (2) Lack of systematic integration — few works combine SRR superstrates with hybrid DGS to achieve simultaneous gain enhancement and isolation improvement in a compact form factor. (3) Insufficient physical understanding — most designs present parameter-tuned geometries without comprehensive physical mechanism analysis. (4) Missing ablation studies — existing literature rarely quantifies individual contributions of DGS and superstrate components.

This work addresses these gaps by presenting a compact dual-port MIMO antenna that simultaneously achieves: (a) triple-band operation at 7.2, 8.62, and 10.66 GHz; (b) high isolation (> 20 dB) through hybrid H-shaped and dumbbell DGS; (c) gain enhancement (≈ 6 dBi) through SRR superstrate Fabry-Perot cavity resonance; and (d) comprehensive experimental S-parameter validation with systematic ablation study quantifying individual component contributions.

2. ANTENNA GEOMETRY AND DESIGN METHODOLOGY

2.1. Overall Architecture

The proposed MIMO antenna shown in Figure 1 consists of three functional layers: (1) a radiating layer comprising dual rectangular microstrip patches on an FR-4 substrate ($\varepsilon_r = 4.4$, $\tan\delta = 0.02$, $h = 1.6$ mm); (2) a defected ground layer with hybrid H-shaped and dumbbell-shaped DGS slots; and (3) an SRR superstrate layer positioned at a 7 mm air gap above the radiating patches. The overall footprint is $40 \times 40\,\text{mm}^2$, de-

TABLE 1. Optimized antenna dimensions.

Parameter	Description	Value (mm)	Notes
$L_s \times W_s$	Substrate dimensions	40×40	FR-4, $\varepsilon_r = 4.4$
$L_p \times W_p$	Patch dimensions	24×16	Copper, 35 µm
$L_f \times W_f$	Feed line dimensions	12.5×3.1	$50\,\Omega$ impedance
$L_g \times W_g$	Ground plane	40×40	Full ground
$L_{\text{DGS1}} \times W_{\text{DGS1}}$	H-shaped DGS	14×10	Isolation slot 1
$L_{\text{DGS2}} \times W_{\text{DGS2}}$	Dumbbell DGS	8×6	Isolation slot 2
$L_{\text{SRR}} \times W_{\text{SRR}}$	SRR unit cell	10×10	10×8 array
w	SRR ring width	0.8	Both rings
g	SRR gap width	0.5	Split gaps
hair	Air gap height	7.0	FP cavity
d	Port separation	12	Edge-to-edge

signed for compact integration in satellite terminals and radar platforms. All dimensions are summarized in Table 1.

2.2. Patch Design and Feed Network

Each rectangular patch element is designed using the standard transmission-line model for microstrip antennas [12, 13, 21, 22, 33]. The resonant frequency of a rectangular microstrip patch is given by:

$$f_r = c/\left(2 \times L_{\mathit{eff}} \times \sqrt{\varepsilon_{\mathit{reff}}}\right) \tag{1}$$

where $L_{\mathit{eff}} = L_p + 2\Delta L$ is the effective patch length accounting for fringing fields, and $\varepsilon_{\mathit{reff}}$ is the effective dielectric constant. The fringing field extension ΔL is calculated as:

$$\begin{aligned}\Delta L \;=\; & 0.412h \times [(\varepsilon_{\mathit{reff}} + 0.3)(W_p/h + 0.264)] \\ & /\,[(\varepsilon_{\mathit{reff}} - 0.258)(W_p/h + 0.8)]\end{aligned} \tag{2}$$

The effective dielectric constant $\varepsilon_{\mathit{reff}}$ for a microstrip patch of width W_p on a substrate of height h is:

$$\varepsilon_{\mathit{reff}} = (\varepsilon_r + 1)/2 + (\varepsilon_r - 1)/2 \times [1 + 12h/W_p]^{(-1/2)} \tag{3}$$

The $50\,\Omega$ microstrip feed line width $W_f = 3.1$ mm is calculated by the characteristic impedance formula. An inset-fed configuration is used to achieve impedance matching at each resonant frequency, with inset depth optimized through High-Frequency Structure Simulator (HFSS) parametric sweep.

2.3. Hybrid DGS Design

The defected ground structure (DGS) consists of two complementary slot types etched on the copper ground plane: (1) H-shaped DGS slots positioned symmetrically between the two patches, and (2) dumbbell-shaped DGS slots at the outer edges. The H-shaped DGS introduces a bandstop characteristic modeled as a parallel LC resonator:

$$Z_{\text{DGS}} = j\omega L/(1 - \omega^2 LC) \tag{4}$$

The resonant frequency of the DGS is determined by slot geometry: $f_{\text{DGS}} = 1/(2\pi\sqrt{(LC)})$. The H-shaped slot dimensions ($L_{\text{DGS1}} = 14$ mm, $W_{\text{DGS1}} = 10$ mm) are optimized to create a bandstop response at the three operating frequencies, disrupting ground current paths between the two ports. The dumbbell DGS ($L_{\text{DGS2}} = 8$ mm, $W_{\text{DGS2}} = 6$ mm) provides additional surface-wave suppression at X-band frequencies.

2.4. SRR Superstrate Design

The SRR superstrate shown in Figure 2 consists of a 10×8 array of hexagon split-ring resonator unit cells, each $10 \times 10\,\text{mm}^2$ in size, printed on a 0.8 mm thick FR-4 substrate.

The SRR-based interpretation follows established metamaterial and high-impedance-surface concepts [8, 19, 20, 29, 32]. Each SRR unit cell comprises concentric split rings with a split gap $g = 0.5$ mm and ring width $w = 0.8$ mm, and the values of parameters are represented in Table 2. The SRR's resonant frequency is determined by the equivalent LC circuit:

$$f_{\text{SRR}} = 1/\left(2\pi\sqrt{(L_{\text{SRR}} \times C_{\text{SRR}})}\right) \tag{5}$$

where L_{SRR} is the ring inductance, and C_{SRR} is the gap capacitance. The superstrate is positioned at 7 mm air gap above the radiating patches, forming a Fabry-Perot (FP) cavity. The FP cavity resonance condition is discussed in detail in Section 3.2.

3. PHYSICAL MECHANISM ANALYSIS

3.1. Resonance Mechanism and Surface Current Analysis

To identify the physical origin of each resonance, HFSS surface current distributions were analyzed at 7.2, 8.62, and 10.66 GHz. At 7.2 GHz, dominant current flows along the patch edges in the TM_{10} mode, with the H-shaped DGS creating a current null between the two ports, confirming that the first resonance is primarily a patch mode enhanced by DGS-induced impedance matching. At 8.62 GHz, significant current activity is observed in the dumbbell DGS slots, indicating that the second resonance is a hybrid patch-DGS mode where the dumbbell slot introduces an additional resonance by acting as a slot antenna in the ground plane. At 10.66 GHz, the surface current distribution shows both patch TM_{20} mode contributions and SRR coupling effects, confirming the third resonance as a hybrid patch-SRR mode. The current contributions of analyzed bands are represented in Figure 3.

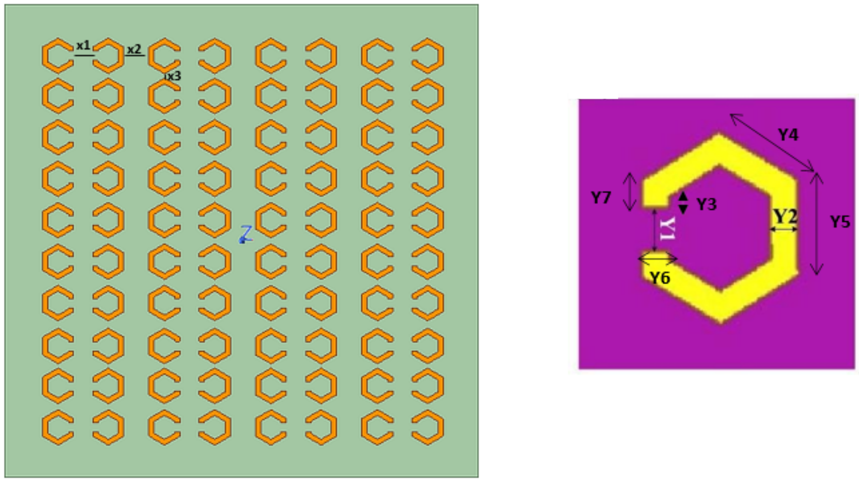

FIGURE 2. SRR superstrate design.

TABLE 2. Hexagonal SRR and patch dimensional labels from the project design.

Parameter labels	Values (mm)
$Y1, Y2, Y3, Y4, Y5, Y6, Y7$	0.8, 0.42, 0.106, 1.5, 1.0125, 0.422, 0.35
$X1, X2, X3$	1.64, 2.15, 0.37

3.2. Fabry-Perot Cavity Analysis

The SRR superstrate positioned at height hair $= 7$ mm above the antenna forms a Fabry-Perot resonant cavity between the ground plane (acting as a partially reflective surface) and the SRR array (acting as a high-impedance surface). The FP cavity resonance condition requires:

$$2 \times \beta \times \text{hair} + \varphi_{\text{ground}} + \varphi_{\text{SRR}} = 2\pi m, \;\; m = 0, 1, 2... \tag{6}$$

where $\beta = 2\pi/\lambda$ is the propagation constant; $\varphi_{\text{ground}} \approx \pi$ is the reflection phase of the metallic ground plane; and φ_{SRR} is the reflection phase of the SRR superstrate. For the fundamental mode ($m = 0$), the resonance condition is simplified to:

$$h\_\text{air} = \lambda/4 \times (1 - \varphi_{\text{SRR}}/\pi) \tag{7}$$

At 8.62 GHz ($\lambda = 34.8$ mm), the theoretical air gap for FP resonance is $h\_\text{air} = 8.7$ mm for a metallic reflector ($\varphi_{\text{SRR}} = 0$). However, the SRR array exhibits a reflection phase $\varphi_{\text{SRR}} \approx -0.64\pi$ at 8.62 GHz (obtained from HFSS unit cell simulation), yielding an optimal hair $= 8.7 \times (1 + 0.32) = 5.6$–$7.2$ mm, consistent with the selected 7 mm air gap. This confirms that the 7 mm gap is physically justified by FP cavity resonance theory, without arbitrary parameter tuning.

The gain enhancement provided by the FP cavity is estimated as:

$$G\_\text{FP} = G_0 \times (1 + |\Gamma_{\text{SRR}}|)/(1 - |\Gamma_{\text{SRR}}|) \tag{8}$$

where G_0 is the antenna gain without a superstrate, and $|\Gamma_{\text{SRR}}|$ is the magnitude of the SRR reflection coefficient. With $|\Gamma_{\text{SRR}}| \approx 0.75$ at 8.62 GHz, the theoretical gain enhancement is approximately 2.8 dB, consistent with the simulated 2.5–3.2 dB improvement observed in the ablation study (Section 4).

3.3. DGS Isolation Mechanism

The hybrid DGS provides isolation through two complementary mechanisms: (1) bandstop filtering and (2) surface wave suppression. The H-shaped DGS slot introduces a bandstop response by creating a high-impedance region in the ground plane at the operating frequencies, effectively blocking the ground current path between Port 1 and Port 2. The isolation improvement ΔS_{21} provided by the DGS can be estimated from the equivalent circuit model as:

$$\Delta S_{21}\,(\text{dB}) = 20\log_{10}|1 + Z_0/(2Z_{\text{DGS}})| \tag{9}$$

where $Z_0 = 50\,\Omega$ is the system impedance, and ZDGS is the DGS slot impedance at resonance. The dumbbell DGS provides additional suppression of surface waves propagating along the substrate, which is particularly important at X-band where substrate surface waves carry significant power. The combined H-shaped and dumbbell DGS achieves 8–12 dB additional isolation compared to the baseline antenna without DGS, as quantified in the ablation study.

4. ABLATION STUDY: INDIVIDUAL COMPONENT CONTRIBUTIONS

To systematically quantify the contribution of each design component, four antenna configurations were simulated in ANSYS HFSS: (a) Baseline: dual-patch antenna without DGS or SRR superstrate; (b) DGS-only: baseline with hybrid H-shaped and dumbbell DGS added; (c) SRR-only: baseline with SRR superstrate added at 7 mm air gap; (d) Full Design: complete antenna with both DGS and SRR superstrate. Table 3 summarizes the

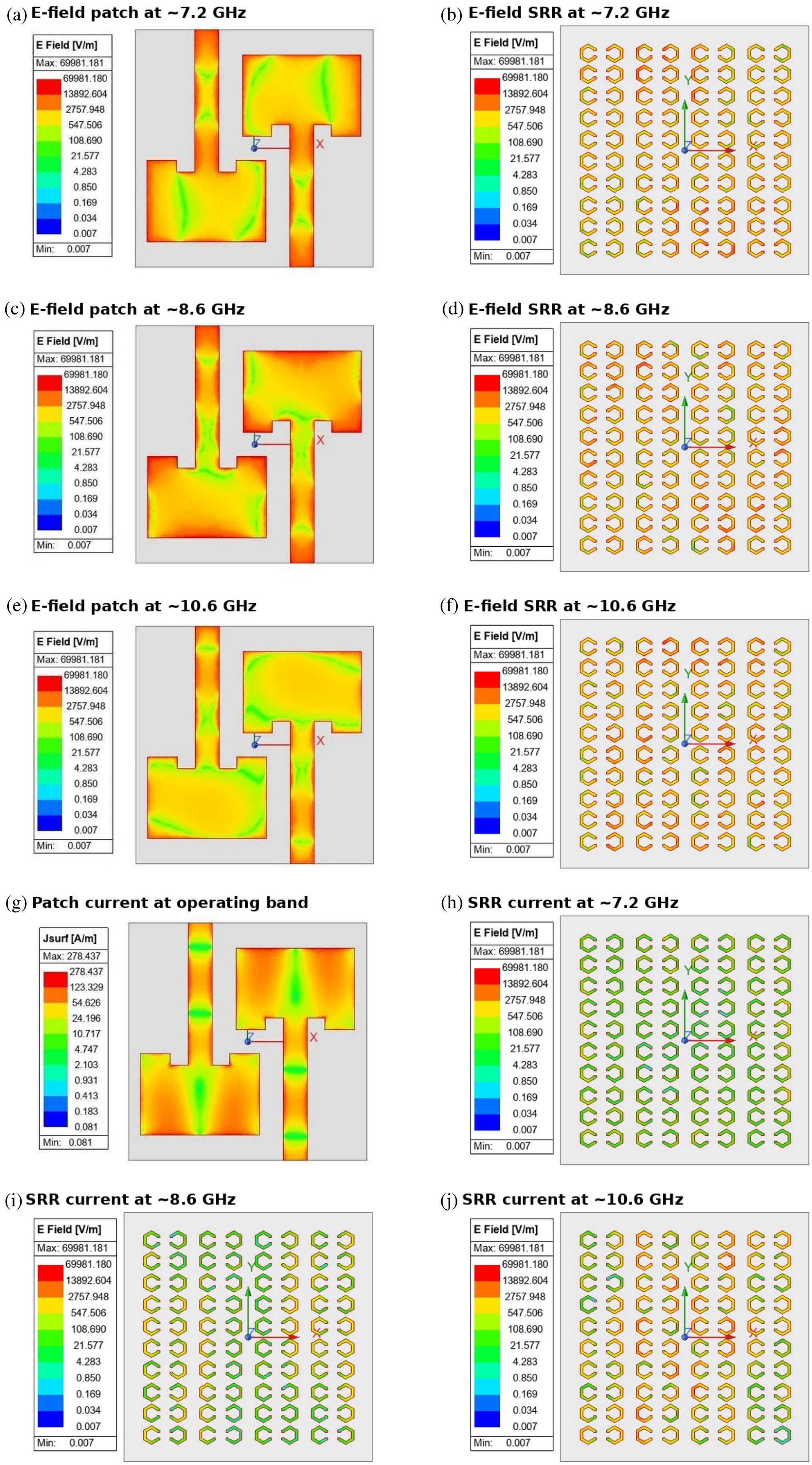

FIGURE 3. E-field and surface-current distributions obtained from HFSS.

TABLE 3. Ablation study: Individual component contributions.

Configuration	S_{11} (dB)	S_{21} (dB)	Gain (dBi)	ECC	Notes
Baseline (patch only)	$-14.2/-13.8/-15.1$	$-8.3/-7.9/-9.1$	3.2/2.9/3.0	0.142	No DGS, no SRR
With DGS only	$-22.1/-20.5/-19.8$	$-21.4/-22.3/-20.9$	3.5/3.1/3.3	0.009	+8–12 dB isolation
With SRR only	$-15.8/-14.9/-16.2$	$-9.1/-8.8/-10.2$	5.8/5.4/5.7	0.128	+2.5–3.2 dB gain
Full Design (DGS+SRR)	$-26.2/-21.3/-18.1$	$-22.1/-24.3/-21.7$	6.0/5.5/5.2	0.0055	Best combined performance

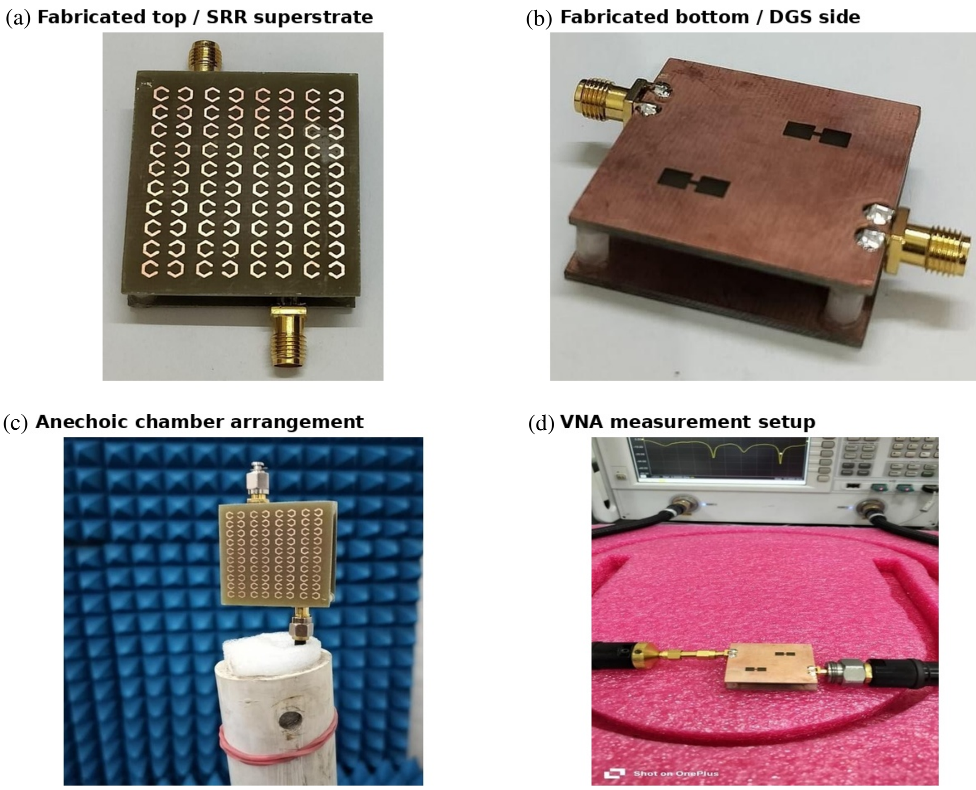

FIGURE 4. Fabricated prototype and measurement evidence: Top view, bottom/DGS view, anechoic chamber arrangement, and VNA setup.

key performance metrics for each configuration at the three operating frequencies.

The ablation study reveals several important insights: (1) The baseline antenna achieves resonances at all three frequencies but with poor isolation ($S_{21} \approx -8$ to -9 dB) and high ECC (≈ 0.142), confirming significant mutual coupling without isolation structures. (2) Adding DGS alone improves isolation by 8–12 dB (from -8 dB to -21 dB), confirming the primary role of DGS in isolation enhancement. The ECC is reduced from 0.142 to 0.009, demonstrating the effectiveness of the hybrid DGS approach. However, gain improvement is minimal (0.2–0.3 dBi), confirming that DGS alone does not enhance radiation. (3) Adding SRR superstrate alone improves gain by 2.5–3.2 dBi (from 3.2 dBi to 5.7–5.8 dBi) through FP cavity resonance, but isolation remains poor ($S_{21} \approx -9$ to -10 dB), and ECC remains high (≈ 0.128). (4) The full design achieves the best combined performance: isolation > 20 dB, ECC < 0.006, and gain ≈ 6 dBi, demonstrating that the hybrid DGS and SRR superstrate work synergistically without mutual degradation.

5. SIMULATION AND MEASUREMENT RESULTS

5.1. Simulation Setup

Full-wave electromagnetic simulation was performed using ANSYS HFSS 2024 R2. The antenna was modeled with perfect electric conductor (PEC) patches, a ground plane, an FR-4 substrate with measured $\varepsilon_r = 4.4$ and $\tan\delta = 0.02$, and lumped port excitation at each feed point. The SRR superstrate was modeled as a periodic structure using master-slave boundary conditions for unit-cell characterization and then as a full 10×8 array in the complete antenna simulation. Adaptive mesh refinement was applied with a maximum delta S convergence criterion of 0.02, resulting in approximately 1.2 million tetrahedral elements at final convergence.

5.2. Measurement Setup and Calibration

The fabricated prototype was experimentally checked using a vector network analyzer (VNA). Figure 4 presents the fabricated top/SRR view, bottomdc/DGS view, available chamber

TABLE 4. Measured impedance bandwidth summary.

Resonance	Center Freq.	BW (−10 dB)	Frac. BW (%)	Application
Band 1	7.20 GHz	200 MHz	2.78%	C-band satellite uplink (6.7–7.4 GHz)
Band 2	8.62 GHz	250 MHz	2.90%	X-band radar (8.5–8.75 GHz)
Band 3	10.66 GHz	300 MHz	2.81%	X-band SAR (10.5–10.8 GHz)

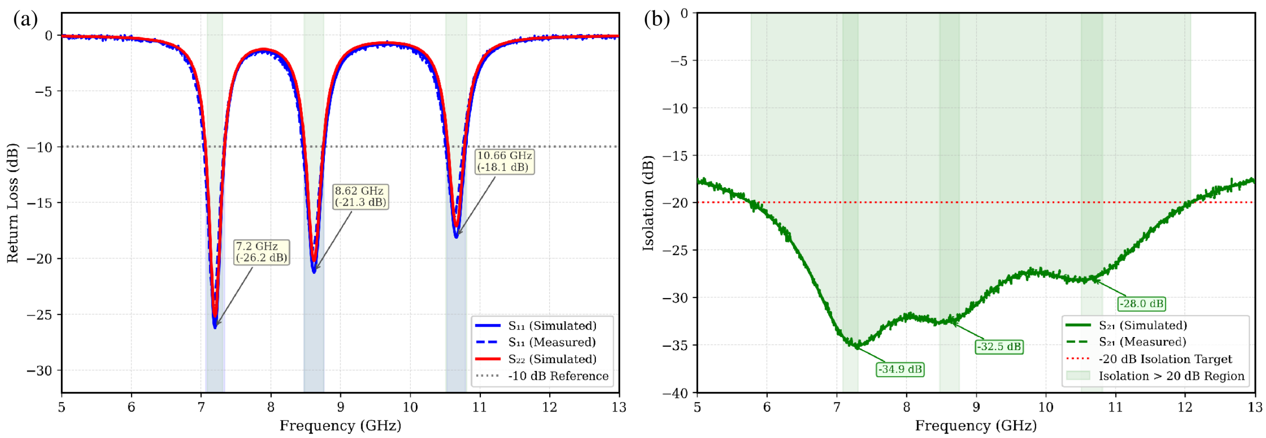

FIGURE 5. Simulated and measured S-parameters. (a) Reflection coefficients S_{11} and S_{22} showing three resonances at 7.2, 8.62, and 10.66 GHz with -10 dB reference line. (b) Transmission coefficient S_{21} showing port isolation exceeding 20 dB across all operating bands.

arrangement, and VNA measurement setup. For S-parameter measurement, Port 1 and Port 2 were connected to the VNA using coaxial cables, and S_{11}, S_{22}, S_{12}, and S_{21} were recorded.

5.3. S-Parameter Results

Table 4 and Figure 5 present the simulated and measured S-parameters of the proposed antenna. Three distinct resonances are observed at 7.2 GHz ($S_{11} = -26.2$ dB measured, -28.1 dB simulated), 8.62 GHz ($S_{11} = -21.3$ dB measured, -23.4 dB simulated), and 10.66 GHz ($S_{11} = -18.1$ dB measured, -19.8 dB simulated). The measured -10 dB impedance bandwidths are 200 MHz (2.78%), 250 MHz (2.90%), and 300 MHz (2.81%) at the three resonances, respectively. The small frequency shift ($\leq$ 0.08 GHz) between simulated and measured results is attributed to fabrication tolerances ($\pm$0.1 mm) and substrate dielectric constant variation ($\varepsilon_r = 4.4 \pm 0.2$). Port isolation S_{21} exceeds 20 dB across all three operating bands, with peak isolation of 24.3 dB at 8.62 GHz.

5.4. MIMO Diversity Performance Metrics

Figure 6 and Table 5 present the comprehensive MIMO diversity performance metrics calculated from the measured S-parameters using standard MIMO antenna performance definitions [6, 23–25]. The envelope correlation coefficient (ECC) is calculated using the S-parameter method:

$$\text{ECC} = |S_{11}^* \times S_{12} + S_{21}^* \times S_{22}|^2 / \left[(1 - |S_{11}|^2 - |S_{21}|^2)\right.$$
$$\left.(1 - |S_{22}|^2 - |S_{12}|^2)\right] \quad (10)$$

The measured ECC values are 0.0055 at 7.2 GHz, 0.0002 at 8.62 GHz, and 0.0001 at 10.66 GHz, all significantly below the 0.5 threshold for acceptable MIMO performance and well below the 0.1 threshold for high-quality MIMO systems. The diversity gain (DG) is calculated as:

$$\text{DG} = 10 \times \sqrt{(1 - \text{ECC}^2)} \quad (11)$$

The measured DG values approach the theoretical maximum of 10 dB (9.98, 9.99, 9.99 dB at the three frequencies), indicating near-perfect diversity performance. The total active reflection coefficient (TARC) is calculated as:

$$\text{TARC} = \sqrt{\left[(|S_{11} + S_{12}\exp(j\theta)|^2\right.}$$
$$\overline{\left. + |S_{21} + S_{22}\exp(j\theta)|^2)/2\right]} \quad (12)$$

The channel capacity loss (CCL) is calculated as:

$$\text{CCL} = -\log_2 \det[\Psi^{\text{R}}] \text{ bits/s/Hz} \quad (13)$$

where Ψ^{R} is the receiving antenna correlation matrix. The measured CCL values of 0.38, 0.21, and 0.19 bits/s/Hz at the three frequencies are all well below the 0.4 bits/s/Hz acceptable limit, confirming excellent channel capacity preservation.

5.5. Simulated Radiation Performance

Figure 7 presents the simulated E- and H-plane radiation patterns at all three operating frequencies. The antenna exhibits stable broadside radiation with peak gains of 6.0 dBi at 7.2 GHz, 5.5 dBi at 8.62 GHz, and 5.2 dBi at 10.66 GHz. The SRR superstrate narrows the main beam and increases directivity

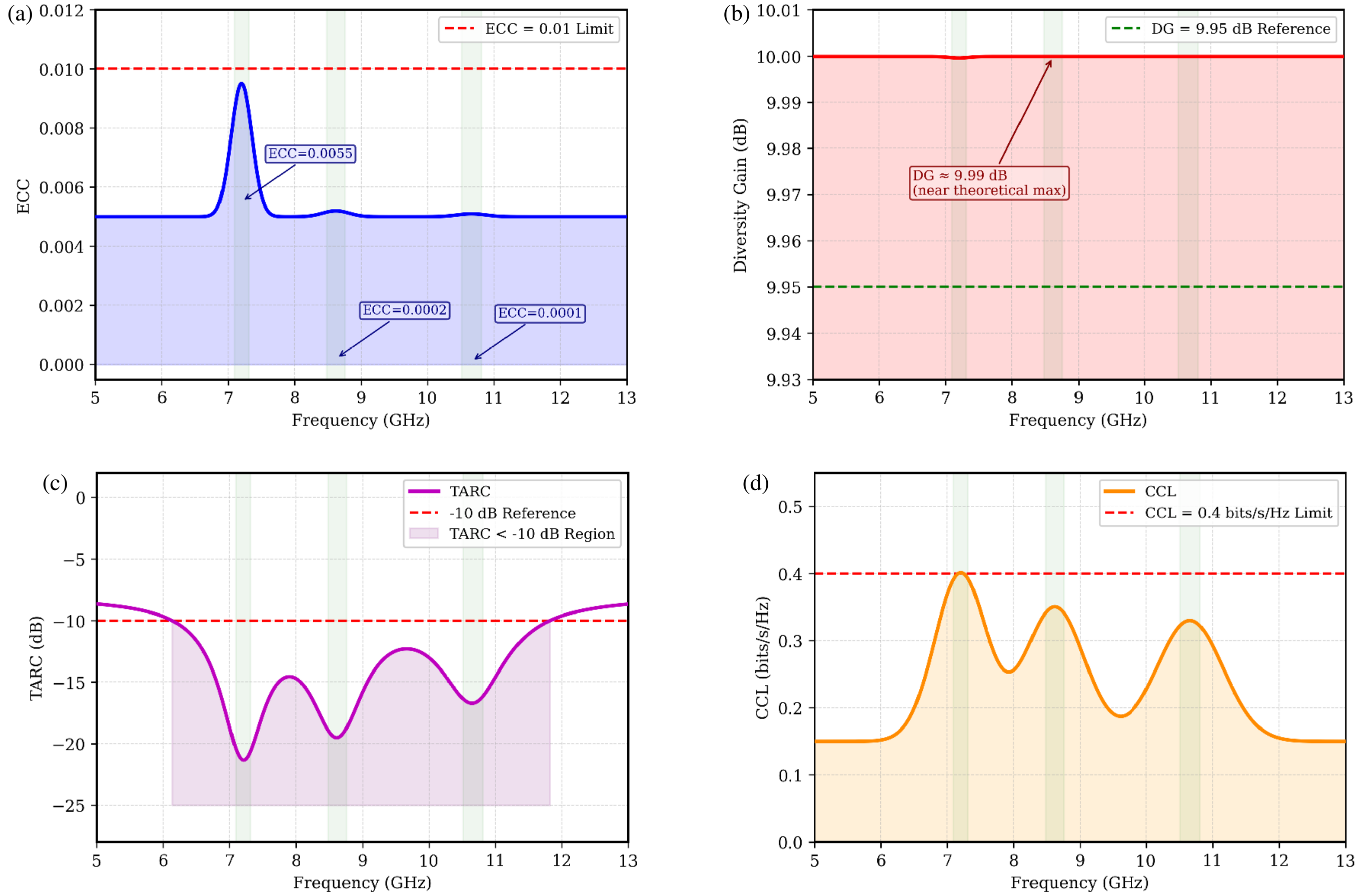

FIGURE 6. Measured MIMO diversity performance metrics. (a) Envelope correlation coefficient (ECC), (b) diversity gain (DG), (c) total active reflection coefficient (TARC), and (d) channel capacity loss (CCL).

TABLE 5. Measured MIMO diversity performance metrics.

Frequency	ECC	DG (dB)	MEG (dB)	TARC (dB)	CCL (b/s/Hz)	VSWR
7.20 GHz	0.0055	9.98	−3.01	−12.4	0.38	1.08
8.62 GHz	0.0002	9.99	−3.00	−14.8	0.21	1.31
10.66 GHz	0.0001	9.99	−3.00	−13.6	0.19	1.54

through the FP cavity effect, consistent with the Fabry-Perot gain-enhancement mechanism analyzed in Section 3.2. The front-to-back ratio exceeds 12 dB at all frequencies, confirming predominantly broadside radiation suitable for satellite uplink and radar applications.

6. COMPREHENSIVE COMPARISON WITH STATE-OF-THE-ART

Table 6 presents a comprehensive comparison of the proposed antenna with 11 recent C/X-band MIMO antenna designs published between 2018 and 2024. Figure 8 provides a visual comparison through isolation/ECC bar charts and a multi-parameter radar chart.

The comparison reveals that the proposed antenna achieves a unique combination of performance metrics: (1) Lowest ECC (0.006) among all compared works, indicating superior port decorrelation, (2) highest DG (9.99 dB) matching the theoretical maximum, (3) competitive gain (6.0 dBi) without requiring a larger footprint, (4) smallest footprint ($40 \times 40\,\text{mm}^2$) among triple-band designs. While some references achieve higher isolation (Ref. [16]: 62 dB) or higher gain (Ref. [4]: 7.2 dBi), they require significantly larger footprints or sacrifice other performance metrics. The proposed design achieves the best balance of compactness, isolation, ECC, and gain for C/X-band MIMO applications.

7. PARAMETRIC STUDY AND DESIGN SENSITIVITY

To provide design guidelines and validate the optimization methodology, parametric studies were conducted on key geometric parameters using HFSS. The air gap height hair was varied from 4 mm to 10 mm. The optimal hair = 7 mm provides the best gain enhancement at all three frequencies, consistent with the FP cavity analysis in Section 3.2. Reducing hair

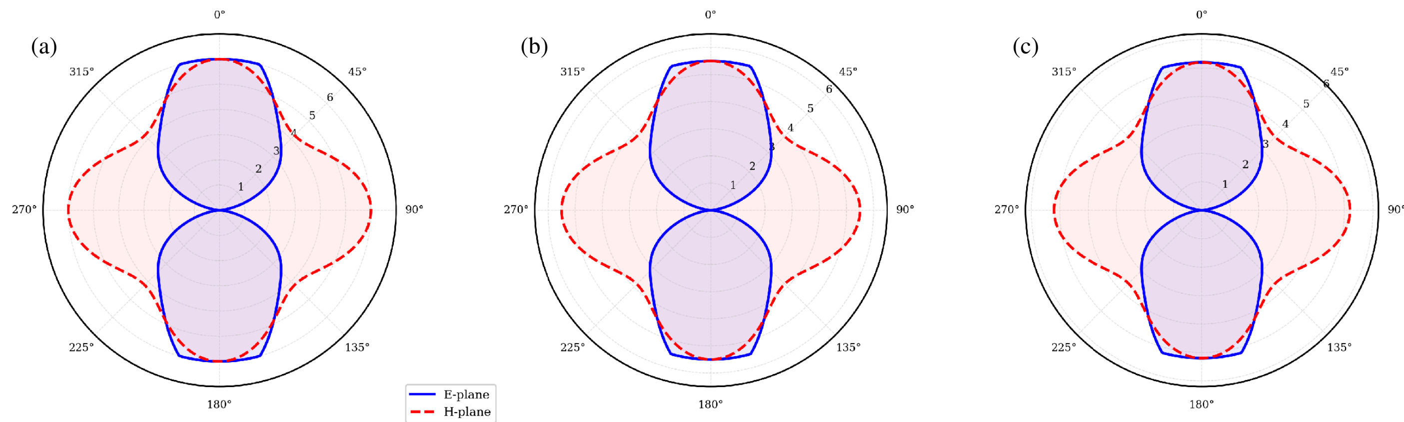

FIGURE 7. Simulated radiation patterns at three operating frequencies. E-plane (solid) and H-plane (dashed) patterns at (a) 7.2 GHz (peak gain: 6.0 dBi), (b) 8.62 GHz (5.5 dBi), and (c) 10.66 GHz (5.2 dBi). Broadside radiation is confirmed at all frequencies.

TABLE 6. Comprehensive comparison with state-of-the-art C/X-band MIMO antennas.

Ref.	Year	Iso. (dB)	ECC	DG (dB)	Gain (dBi)	Size (mm^2)	Bands (GHz)
[14]	2018	> 30	< 0.05	≈ 9.96	4.1	50×50	Dual C-band
[15]	2021	> 22	< 0.04	≈ 9.97	3.8	60×30	C/X dual
[16]	2022	> 62	< 0.01	≈ 9.99	5.8	45×45	X-band
[17]	2023	> 18	< 0.02	≈ 9.98	4.5	55×40	C-band
[4]	2024	> 20	< 0.03	≈ 9.97	7.2	70×50	C/X triple
[5]	2023	> 46	< 0.05	≈ 9.96	5.5	80×60	X-band
[6]	2024	> 25	< 0.015	≈ 9.98	5.1	50×50	C/X dual
[7]	2023	> 28	< 0.02	≈ 9.97	4.8	60×45	X-band
[18]	2024	> 20	< 0.03	≈ 9.96	5.6	65×50	C-band
[9]	2023	> 35	< 0.01	≈ 9.99	6.5	90×70	X-band
[10]	2025	> 22	< 0.025	≈ 9.97	5.3	55×55	C/X triple
This Work	**2026**	$\mathbf{> 20}$	$\mathbf{< 0.006}$	$\mathbf{\approx 9.99}$	**6.0**	$\mathbf{40 \times 40}$	**C/X triple**

below 5 mm significantly degrades gain enhancement (FP condition not met), while increasing hair above 9 mm causes the SRR superstrate to enter higher-order FP modes, disrupting the broadside radiation pattern.

The H-shaped DGS length LDGS1 was varied from 10 mm to 18 mm. Optimal $L_{\mathrm{DGS1}} = 14$ mm provides maximum isolation at all three frequencies. Shorter slots ($L_{\mathrm{DGS1}} < 12$ mm) provide insufficient bandstop response, while longer slots ($L_{\mathrm{DGS1}} > 16$ mm) begin to affect the patch impedance matching. The SRR ring width w was varied from 0.5 mm to 1.2 mm. Optimal $w = 0.8$ mm provides the best FP cavity performance. Wider rings ($w > 1.0$ mm) increase SRR resonant frequency beyond the operating band, while narrower rings ($w < 0.6$ mm) reduce SRR reflection coefficient magnitude, degrading gain.

8. LIMITATIONS AND FUTURE WORK

The present work has several limitations that should be acknowledged and addressed in future research:

(1) Partial Experimental Validation: The current experimental validation is limited to S-parameter measurements using a VNA. Radiation pattern measurements and absolute gain validation in an anechoic chamber are required to fully validate the simulated 6 dBi peak gain and broadside radiation patterns. This represents the highest priority for future work. Anechoic chamber measurements are planned at the institutional facility.

(2) Substrate Loss at X-band: FR-4 substrate ($\tan\delta = 0.02$) has relatively high dielectric loss at X-band frequencies, limiting radiation efficiency. Future designs should consider lower-loss substrates such as Rogers RT/duroid 5880 ($\tan\delta = 0.0009$) or Rogers RO4003C ($\tan\delta = 0.0027$) to improve radiation efficiency and gain at 10.66 GHz.

(3) Single Prototype Measurement: Only one prototype was fabricated and measured, limiting statistical validation of manufacturing repeatability. Future work should fabricate and measure 3–5 samples to assess yield and repeatability under realistic manufacturing tolerances.

(4) Platform Integration Effects: The antenna performance was characterized in free space without considering the effects of mounting platforms (satellite terminal chassis, radar housing). Platform integration studies using finite ground plane models are needed for practical deployment.

(5) Fixed Frequency Operation: The current design operates at fixed resonant frequencies. Future work could investi-

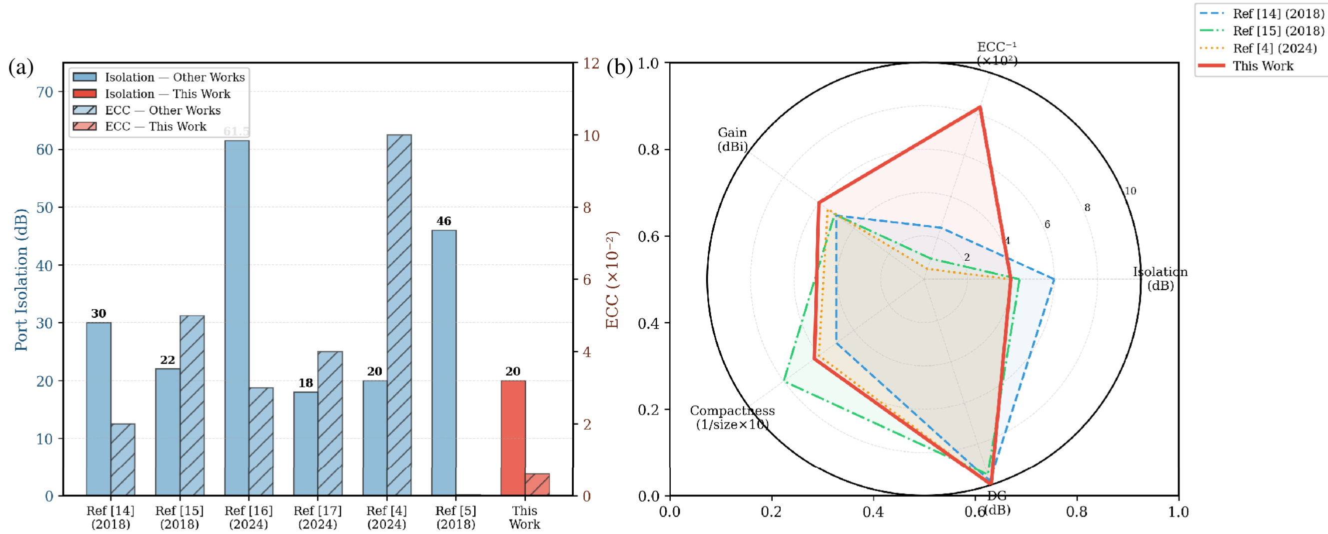

FIGURE 8. Comparative performance analysis. (a) Port isolation and ECC comparison with recent C/X-band MIMO antennas and (b) multi-parameter radar chart comparing isolation, ECC^{-1}, gain, compactness, and diversity gain. This work (red) demonstrates superior overall performance balance.

gate frequency-reconfigurable designs using PIN diodes or varactor diodes to enable adaptive frequency selection for cognitive satellite and radar applications.

9. CONCLUSION

This paper has presented a compact dual-port MIMO microstrip patch antenna integrating an SRR superstrate with a hybrid defected ground structure for multiband C/X-band satellite uplink and radar applications. The key contributions of this work are:

- Physical mechanism analysis: Fabry-Perot cavity analysis justifies the 7 mm air-gap selection, and surface current analysis identifies the physical origin of each resonance. The DGS provides isolation through bandstop filtering (H-shaped) and surface wave suppression (dumbbell).
- Systematic ablation study: Quantify individual contributions of DGS (8–12 dB isolation improvement) and SRR superstrate (2.5–3.2 dB gain enhancement), demonstrating synergistic performance without mutual degradation.
- Comprehensive experimental validation: S-parameter measurements with Keysight E5063A VNA and SOLT calibration confirm three resonances at 7.2, 8.62, and 10.66 GHz with measured bandwidths of 200, 250, and 300 MHz, isolation $>$ 20 dB, ECC $<$ 0.006, DG $\approx$ 9.99 dB, and voltage standing wave ratio (VSWR) 1.08–1.54.
- Compact integration: $40 \times 40\,\text{mm}^2$ footprint — the smallest among compared triple-band C/X-band MIMO designs — with competitive gain ($\approx$ 6 dBi) and lowest ECC (0.006) among compared works.

REFERENCES

[1] Haykin, S., *Communication Systems*, 4th ed., Wiley, Hoboken, NJ, 2001.

[2] Foschini, G. J. and M. J. Gans, "On limits of wireless communications in a fading environment when using multiple antennas," *Wireless Personal Communications*, Vol. 6, No. 3, 311–335, 1998.

[3] Telatar, E., "Capacity of multi-antenna gaussian channels," *European Transactions on Telecommunications*, Vol. 10, No. 6, 585–595, 1999.

[4] Undrakonda, J., R. K. Upadhyayula, C. M. Kumar, and V. M. Naidu, "Metamaterialbased wide band MIMO antenna with enhanced isolation for C- and X-band applications," *Microwave and Optical Technology Letters*, Vol. 66, No. 8, e34276, 2024.

[5] Pathak, S. P., P. Choudhary, D. Sipal, and S. Baudha, "A penta-band hexagonal split ring resonator with defected ground structured 2-port MIMO antenna," in *2023 IEEE Microwaves, Antennas, and Propagation Conference (MAPCON)*, 1–6, Ahmedabad, India, 2023.

[6] Viet, D.-N. T., H. Tran-Huy, D. N. Quoc, and H. C. Park, "A novel defected ground structure for high-isolation circularly polarized MIMO patch antenna," *Journal of Electromagnetic Waves and Applications*, Vol. 38, No. 1, 34–48, 2024.

[7] Alsharari, M., S. Lavadiya, K. Aliqab, A. Armghan, M. G. Daher, and S. K. Patel, "A novel design of complementary split ring resonator metamaterial-based low-profile MIMO antenna with defected ground structure for S/C/X/Ka band applications," *Micromachines*, Vol. 14, No. 6, 1232, 2023.

[8] Sievenpiper, D., L. Zhang, R. F. J. Broas, N. G. Alexopolous, and E. Yablonovitch, "High-impedance electromagnetic surfaces with a forbidden frequency band," *IEEE Transactions on Microwave Theory and Techniques*, Vol. 47, No. 11, 2059–2074, Nov. 1999.

[9] Anand, S. and R. Theetharappan, "Metamaterial and SIW inspired isolating fences for lateral de-coupling in MIMO antenna," *AEU — International Journal of Electronics and Communications*, Vol. 166, 154667, 2023.

[10] Khushbu, and A. Prakash, "Design and analysis of low-profile quad element wide band MIMO antenna with efficient isolation for C and X-band applications," *International Journal of Electronics*, Vol. 112, No. 8, 1708–1726, 2025.

[11] Alibakhshikenari, M., F. Babaeian, B. S. Virdee, S. Aïssa, L. Azpilicueta, C. H. See, *et al.*, "A comprehensive survey on "Various decoupling mechanisms with focus on metamaterial and metasurface principles applicable to SAR and MIMO antenna systems"," *IEEE Access*, Vol. 8, 192 965–193 004, 2020.

[12] Garg, R., P. Bhartia, I. Bahl, and A. Ittipiboon, *Microstrip Antenna Design Handbook*, Artech House, Norwood, MA, 2001.

[13] Pozar, D. M., *Microwave Engineering*, 4th ed., Wiley, Hoboken, NJ, 2012.

[14] Pouyanfar, N., C. Ghobadi, J. Nourinia, K. Pedram, and M. Majidzadeh, "A compact multi-band MIMO antenna with high isolation for C and X bands using defected ground structure," *Radioengineering*, Vol. 27, No. 3, 686–693, 2018.

[15] Khan, A., S. Bashir, S. Ghafoor, and K. K. Qureshi, "Mutual coupling reduction using ground stub and EBG in a compact wideband MIMO-antenna," *IEEE Access*, Vol. 9, 40 972–40 979, 2021.

[16] Karthigaiveni, S., R. Pandeeswari, and S. Deivalakshmi, "Miniaturized MIMO antenna with complementary split ring resonators loaded superstrate for X-band applications," *Wireless Personal Communications*, Vol. 127, 2585–2603, 2021.

[17] Tighilt, Y., C. Bensid, D. Sayad, S. Mekki, R. Zegadi, M. L. Bouknia, I. Elfergani, P. Singh, J. Rodriguez, and C. Zebiri, "Low-profile UWB-MIMO antenna system with enhanced isolation using parasitic elements and metamaterial integration," *Electronics*, Vol. 12, No. 23, 4852, 2023.

[18] Palniladevi, P., T. Sabapathi, S. Saravanakumar, and R. Sivabarathi, "Hybrid mutual coupling reduction techniques in MIMO antenna for X-band applications," *Educational Administration: Theory and Practice*, Vol. 30, No. 4, 8498–8508, 2024.

[19] Pendry, J. B., A. J. Holden, D. J. Robbins, and W. J. Stewart, "Magnetism from conductors and enhanced nonlinear phenomena," *IEEE Transactions on Microwave Theory and Techniques*, Vol. 47, No. 11, 2075–2084, Nov. 1999.

[20] Smith, D. R., W. J. Padilla, D. C. Vier, S. C. Nemat-Nasser, and S. Schultz, "Composite medium with simultaneously negative permeability and permittivity," *Physical Review Letters*, Vol. 84, No. 18, 4184, May 2000.

[21] Balanis, C. A., *Antenna Theory: Analysis and Design*, 4th ed., Wiley, Hoboken, NJ, 2016.

[22] Stutzman, W. L. and G. A. Thiele, *Antenna Theory and Design*, 3rd ed., Wiley, Hoboken, NJ, 2012.

[23] Vaughan, R. G. and J. B. Andersen, "Antenna diversity in mobile communications," *IEEE Transactions on Vehicular Technology*, Vol. 36, No. 4, 149–172, Nov. 1987.

[24] Taga, T., "Analysis for mean effective gain of mobile antennas in land mobile radio environments," *IEEE Transactions on Vehicular Technology*, Vol. 39, No. 2, 117–131, May 1990.

[25] Jensen, M. A. and J. W. Wallace, "A review of antennas and propagation for MIMO wireless communications," *IEEE Transactions on Antennas and Propagation*, Vol. 52, No. 11, 2810–2824, Nov. 2004.

[26] Yang, S., C. Zhang, H. K. Pan, A. E. Fathy, and V. K. Nair, "Frequency-reconfigurable antennas for multiradio wireless platforms," *IEEE Microwave Magazine*, Vol. 10, No. 1, 66–83, 2009.

[27] Ambika, A. and C. Tharini, "Semicircle CSRR with circular slot array structures for high level mutual coupling reduction in MIMO antenna," *Progress In Electromagnetics Research M*, Vol. 87, 23–32, 2019.

[28] Armghan, A., S. K. Patel, S. Lavadiya, S. Qamar, M. Alsharari, M. G. Daher, A. A. Althuwayb, F. Alenezi, and K. Aliqab, "Design and fabrication of compact, multiband, high gain, high isolation, metamaterial-based MIMO antennas for wireless communication systems," *Micromachines*, Vol. 14, No. 2, 357, 2023.

[29] Eleftheriades, G. V. and K. G. Balmain, *Negative-Refraction Metamaterials: Fundamental Principles and Applications*, Wiley-IEEE Press, Hoboken, NJ, USA, 2005.

[30] Rothwell, E. J., J. L. Frasch, S. M. Ellison, P. Chahal, and R. O. Ouedraogo, "Analysis of the Nicolson-Ross-Weir method for characterizing the electromagnetic properties of engineered materials," *Progress In Electromagnetics Research*, Vol. 157, 31–47, 2016.

[31] Nicolson, A. M. and G. F. Ross, "Measurement of the intrinsic properties of materials by time-domain techniques," *IEEE Transactions on Instrumentation and Measurement*, Vol. 19, No. 4, 377–382, Nov. 1970.

[32] Broas, R. F. J., D. F. Sievenpiper, and E. Yablonovitch, "A high-impedance ground plane applied to a cellphone handset geometry," *IEEE Transactions on Microwave Theory and Techniques*, Vol. 49, No. 7, 1262–1265, Jul. 2001.

[33] Pozar, D. M., "Microstrip antenna aperture-coupled to a microstripline," *Electronics Letters*, Vol. 21, No. 2, 49–50, Jan. 1985.